Electrochemical Formation Mechanism for the Controlled Synthesis of Heterogeneous MnO_2/Poly(3,4-ethylenedioxythiophene) Nanowires

Ran Liu,[†] Jonathon Duay,[†] and Sang Bok Lee[†,‡,*]

[†]Department of Chemistry and Biochemistry, University of Maryland, College Park, Maryland 20742, United States and [‡]Graduate School of Nanoscience and Technology (WCU), Korea Advanced Institute of Science and Technology, Daejeon 305-701, Korea

ABSTRACT The formation mechanism of a coaxial manganese oxide/poly(3,4-ethylenedioxythiophene) (MnO_2/PEDOT) nanowire is elucidated herein by performing electrodeposition of MnO_2 and PEDOT on Au-sputtered nanoelectrodes with different shapes (ring and flat-top, respectively) within the 200 nm diameter pores of an anodized aluminum oxide (AAO) template. It is found that PEDOT prefers to grow on the sharp edge of the ring-shaped electrode, while MnO_2 is more likely to deposit on the flat-top electrode due to its smooth surface. The formation of coaxial nanowires is shown to be a result of simultaneous growth of core MnO_2 and shell PEDOT by an analysis of the current density resulting from electrochemical deposition. Furthermore, the structures of the MnO_2/PEDOT coaxial nanowires were studied for their application as supercapacitors by modifying their coelectrodeposition potential. A potential of 0.70 V is found to be the most favorable condition for synthesis of MnO_2/PEDOT coaxial nanowires, resulting in a high specific capacitance of 270 F/g. Additionally, other heterogeneous MnO_2/PEDOT nanostructures are produced, such as nanowires consisting of MnO_2 nanodomes with PEDOT crowns as well as segmented MnO_2/PEDOT nanowires. This is accomplished by simply adjusting the parameters of the electrochemical deposition. Finally, in smaller diameter (50 nm) AAO channels, MnO_2 and PEDOT are found to be partially assembled into coaxial nanowires due to the alternative depletion of Mn(II) ions and EDOT monomers in the smaller diameter pores.

KEYWORDS: coaxial nanowires · MnO_2 · PEDOT · heterogeneous · lithium-ion battery · supercapacitor · power density · energy density · electrochemical energy storage · template synthesis

One of the major challenges facing researchers today is to provide highly efficient, low-cost, and environmentally friendly electrical energy storage (EES) devices in order to address the problems of climate change and the approaching exhaustion of fossils fuels.[1−8] The frontier research in EES is focused on electrochemical energy storage devices, such as lithium-ion batteries[1,2,6,7] and supercapacitors[3−5] due to their increased role in our daily lives by powering numerous portable consumer electronic devices (*e.g.*, cell phones, PDAs, laptops) and even hybrid electric vehicles. However, in order to meet the elevated requirements[2,9] (*e.g.*, high power density and high energy density) of future systems such as plug-in hybrid electric vehicles (PHEVs), revolutionary advances such as using innovative materials with architecturally tailored structures are needed.

Nanostructured materials have been intensively investigated for application in electrochemical energy storage because of their high specific surface area and small dimensions. These properties can enhance electron and ion transport, leading to improved charge/discharge capabilities as well as increased energy densities. A few excellent reviews on the application of nanostructured materials in lithium ion batteries and supercapacitors can be found in the literature.[4,10−14] However, nanomaterials composed of a single material may not be able to fulfill the requirements of future EES devices due to inherent material limitations such as low energy densities, slow kinetics (low power densities), poor conductivities, and weak mechanical stabilities.[15,16] These limitations may be overcome by heterogeneous nanostructured materials with multinanocomponents, each tailored to address different demands (*e.g.*, high energy density, high conductivity, and excellent mechanical stability). The resulting materials are expected to exhibit synergic properties from integrating each individual component, realizing the full potential of the materials in terms of performance (*e.g.*, high energy density and high power density).[16−22] The recent advances of using heterogeneous nanostructures in the electrode materials for

* Address correspondence to slee@umd.edu.

Received for review March 23, 2011 and accepted June 10, 2011.

Published online June 10, 2011
10.1021/nn201106j

electrochemical energy storage can be found in our review.[23] The success of applying heterogeneous nanostructured materials in energy storage will hinge on the following factors in particular: (1) selecting a proper combination of materials; (2) design of the heterogeneous nanostructure, for example, coaxial nanowires,[17−19] segmented nanowires, or core−shell nanoparticles;[20,21] and (3) employing proper methods to synthesize these nanocomponents into the desired and proposed nanostructures.

The design of these heterogeneous nanostructures is especially important in enhancing their material properties. One of the ideal nanostructures that have been intensively studied in the field of energy storage is the one-dimensional nanostructure array. These arrays consist of nanostructures whose radically small dimensions can effectively shorten the diffusion lengths of the ions, leading to improved charge/discharge rate capabilities, while the large axial dimension can provide high surface area and sufficient mass loading for electrode materials to store sufficient energy.[24−30] For example, Martin's group has reported enhanced charge transport rates in template-synthesized one-dimensional nanomaterials.[28−31] In addition, nanotubes of RuO_2,[26] PEDOT,[32] and RuO_2/PEDOT composite[33] have been reported for high-power supercapacitors by Hu's group[26] and our group,[32,33] respectively.

Coaxial nanowires or nanotubes have attracted an increasing amount of attention due to the advantages derived from their synergetic properties and functionalities, as well as having benefits from their one-dimensional nanostructure, as mentioned earlier.[17−19] For example, SnO_2−In_2O_3 heterostructured nanowires[19] and coaxial MnO_2/carbon nanotube array electrodes[18] have been reported for high-performance lithium-ion batteries.

Along these lines, we have demonstrated a coaxial MnO_2/PEDOT nanowire array for applications in supercapacitors.[17] The core MnO_2 provides high energy density, while the highly conductive, porous, and flexible PEDOT shell facilitates electron transport and ion diffusion into the core MnO_2 and protects it from structural collapse. These combined properties allow for the realization of very high specific capacitances at high current densities. However, there is an incomplete understanding of the coaxial nanowire formation mechanism as well as insufficient knowledge on how to modify these coaxial nanostructures in order to realize their full potential.

In this paper, we investigate the detailed growth mechanism of coaxial manganese oxide/poly(3,4-ethylenedioxythiophene) (MnO_2/PEDOT) by performing coelectrodeposition of MnO_2 and PEDOT onto sputtered and electrodeposited nanoelectrodes with different shapes within 200 nm anodic alumina oxide (AAO) channels. The shapes of the nanoelectrodes in the AAO are found to have strong selectivity in the formation of MnO_2 and PEDOT: PEDOT is grown preferentially on the sharp edge of the ring-shaped electrodes, while the deposition of MnO_2 is more active on the smooth surface of the flat-top electrodes. The phase segregation of MnO_2 and PEDOT leads to the concurrent growth of core MnO_2 and shell PEDOT creating the coaxial nanowires, which is illuminated by an examination of the current densities resulting from the electrochemical deposition. The structures of the MnO_2/PEDOT coaxial nanowires were improved for applications in supercapacitors by modifying the potential during their coelectrodeposition. MnO_2/PEDOT coaxial nanowires showed the highest specific capacitance of 270 F/g when synthesized at the potential of 0.70 V *vs* Ag/AgCl. Such a high specific capacitance is due to the minimal usage of the PEDOT shell in the coaxial nanowires, which facilitates the condition of high conductivity without decreasing the high capacitive nature of MnO_2. In addition to coaxial nanowires, other heterogeneous MnO_2/PEDOT nanocomposites are fabricated by adjusting various parameters for the electrodeposition. For example, MnO_2 nanodomes covered with PEDOT crowns are grown on flat-top electrodes due to the initial MnO_2 selective deposition on the smooth electrode surface. Segmented MnO_2/PEDOT nanowires are synthesized by simply alternating the electrodeposition potential, while controlling the charge during each potential can alter the length of the MnO_2 and PEDOT segments. Finally, the size of the nanoelectrodes also has strong influence on the structures of MnO_2/PEDOT. Due to the alternative depletion of Mn(II) ions and EDOT monomers in small pore diameter (50 nm) AAO, MnO_2 and PEDOT are found to be partially assembled into coaxial nanowires in the AAO template. MnO_2 nanoparticles and nanofibers with different crystallinity are found to be randomly distributed inside the PEDOT shells.

RESULTS AND DISCUSSION

Effect of Nanoelectrode Shape. In our previous research, a simple growth mechanism was proposed for MnO_2/PEDOT coaxial nanowires: PEDOT preferentially grows as tubes on the sharp edge of sputtered ring-shaped Au electrodes at the bottom of the pores *via* electropolymerization of EDOT,[17,25] while *via* phase segregation, MnO_2 grows as the core, as illustrated in Scheme 1a. In this study, we show experimentally that PEDOT growth is indeed more active on the ring-shaped electrodes due to its sharp edges. In addition, this study leads to a new finding: MnO_2 growth also has its own selectivity between the electrode shapes.

First, MnO_2 and PEDOT's individual growth rate is determined on ring-shaped electrodes and flat-top electrodes using cyclic voltammetry (CV) methods. These experiments were performed using a 10 mM Mn^{2+} solution for the MnO_2 data and an 80 mM EDOT

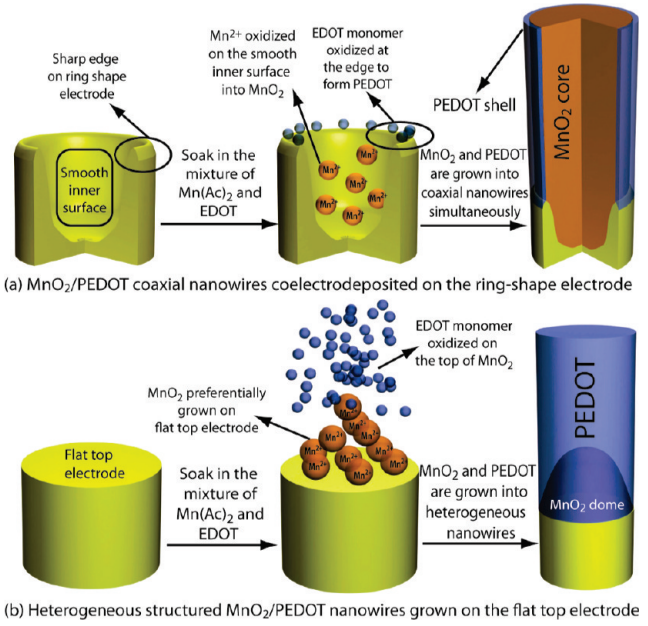

Scheme 1. Growth mechanisms of heterogeneous nanostructured MnO_2/PEDOT by coelectrodeposition of MnO_2 and PEDOT on (a) ring-shaped and (b) flat-top electrodes.

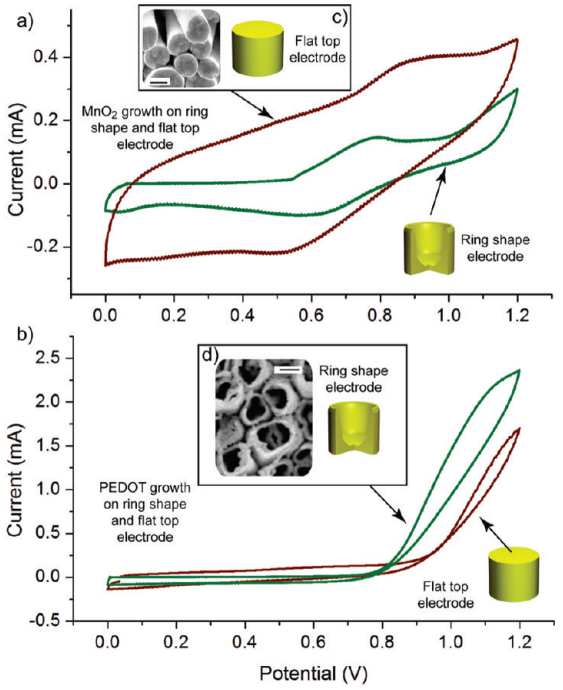

Figure 1. (a) Cyclic voltammetry graphs of MnO_2 (10 mM) growth on ring-shaped electrodes (green) and flat-top electrodes (red) in the alumina template at a scan rate of 100 mV/s from 0 to 1.2 V. (b) Cyclic voltammetry graphs of PEDOT (80 mM) growth on ring-shaped electrodes (green) and flat-top electrodes (red) in the alumina template at a scan rate of 100 mV/s from 0 to 1.2 V. (c,d) SEM images of the flat-top and ring-shaped electrodes, respectively (scale bar = 200 nm).

concentration for the PEDOT data. Figure 1a shows that MnO_2 has a much higher current on the flat-top electrode shown in the inset of Figure 1c. This suggests that the growth of MnO_2 is more active on the smooth-surface electrodes rather than on the ring-shaped electrodes shown in the inset of Figure 1d. This implies that, when MnO_2 and PEDOT are coelectrodeposited, the MnO_2 selectively deposits on the inner smooth surface of the ring-shaped electrode (Scheme 1a) and grows initially in the center of the AAO pore, which is further developed into the MnO_2 core nanowire due to the phase segregation with it and the PEDOT shell. Figure 1b shows the CV graph of PEDOT growth on the ring-shaped electrode and the flat-top electrode. It is

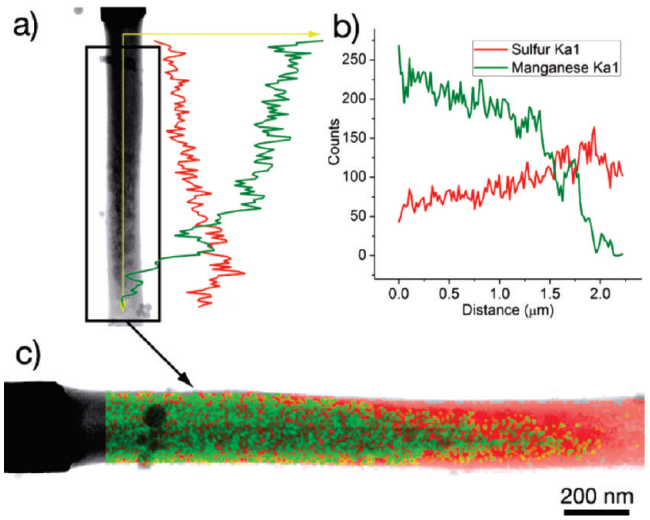

Figure 2. (a) TEM image of a heterostructured MnO_2/PEDOT nanowire grown on a flat Au electrode at 0.85 V (b) Mn (green) and S (red) EDS line scan profiles along the axis of the same nanowire in (a). (c) Mn (green) and S (red) EDS mapping on the framed area in (a).

clear from these results that the growth of PEDOT has a preference for the ring-shaped electrode due to its sharp edge: not only is the resulting growth current on the ring-shaped electrode higher, but the onset growth potential of PEDOT has shifted to a higher value on the flat-top electrode.

The above results provide convincing evidence to support the mechanism of heterogeneous MnO_2/PEDOT coaxial nanowire formation proposed previously.[17]

In order to further solidify the above-mentioned mechanism, we have performed coelectrodeposition of MnO_2 and PEDOT on a flat-top Au electrode as comparative experiments. Flat-top Au electrodes are obtained by the electrodeposition of Au into the gold-sputtered alumina membranes in order to fill in the ring-shaped electrodes, thus creating a flat-top.

Our experimental results show that the nanostructures of the coelectrodeposited MnO_2 and PEDOT on the flat-top electrode are quite different from MnO_2/PEDOT coaxial nanowires synthesized on ring-shaped electrodes. Our previous study showed that PEDOT nanotubes with different thicknesses can be obtained by controlling the potential of electrodeposition from 0.7 to 0.8 V.[17] Lower potentials (0.6−0.65 V) result in the growth of pure MnO_2 nanowires, while higher potentials (0.85 to 1 V) lead to the formation of pure PEDOT nanowires.[17] However, in this paper, no coaxial nanowire growth on the flat-top electrode can be observed.

On the ring-shaped electrode, a potential of 0.75 V leads to the formation of MnO_2/PEDOT coaxial nanowire with a Mn/S molar ratio of approximately 1:1. However, on the flat-top electrode at the same 0.75 V electrodeposition potential, almost pure MnO_2 is grown, and PEDOT shells are not observed when using EDS (data not shown). Further, it was found that only PEDOT can be identified when a potential higher than 0.85 V is applied during the electrodeposition. In this case, the PEDOT is not grown as a uniform shell surrounding the MnO_2 core. Instead, it is grown on the top of a gradually thinning MnO_2 segment, which is always deposited preferentially first on the flat Au electrodes (Scheme 1b).

Figure 2a shows a TEM image of a typical heterostructured MnO_2/PEDOT nanowire grown on a flat-top electrode at 0.85 V. The MnO_2 bottom appears darker than the top PEDOT part.[17] Figure 2b shows the EDS elemental line scan profiles along the axis of this nanowire where Mn represents MnO_2 and S represents PEDOT as the S originates from the sulfur on PEDOT's thiophene ring. The Mn EDS line shows that near the top of the flat electrode, MnO_2 has a much higher concentration than PEDOT. Thereafter, the MnO_2/PEDOT ratio starts to decrease, and the diameter of the MnO_2 segment becomes smaller. The PEDOT concentration shows a precisely opposite trend along the axis. Finally, at the tip of this nanowire, only pure PEDOT is detected.

Figure 2c shows the EDS mapping of Mn and S, which further verifies the distribution of MnO_2 and PEDOT on the heterostructured MnO_2/PEDOT nanowire. This indicates that the flat-top electrode has a strong selectivity for the growth of MnO_2 but not for the growth of PEDOT. Furthermore, although the two electrodes have different shapes (ring-shape and flat-top), the electrolyte ion diffusion toward their surface is similar. In each case, the sizes of the high aspect ratio nanochannels (diameter and length) that determine the electrolyte ion diffusion are identical. On the basis of Figure 1a, under a diffusion-controlled reaction, the ring-shaped electrode is supposed to exhibit a higher current from the electrochemical deposition of MnO_2 due to its higher surface area than flat-top electrodes. However, the resulting current from Mn^{2+} oxidation on the flat-top electrode is larger. This means the flat-top electrode is indeed more active on the MnO_2 electrochemical

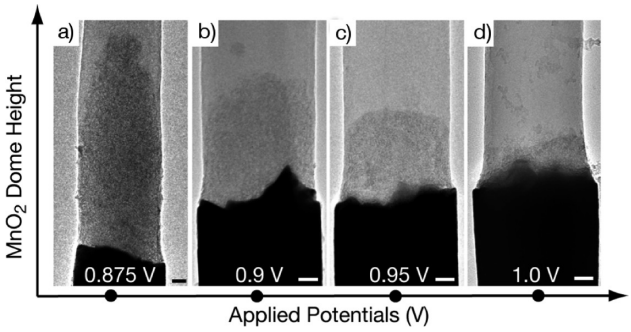

Figure 3. MnO_2 nanodome height *versus* potential applied for electrodeposition of MnO_2 and PEDOT on the flat-top electrode.

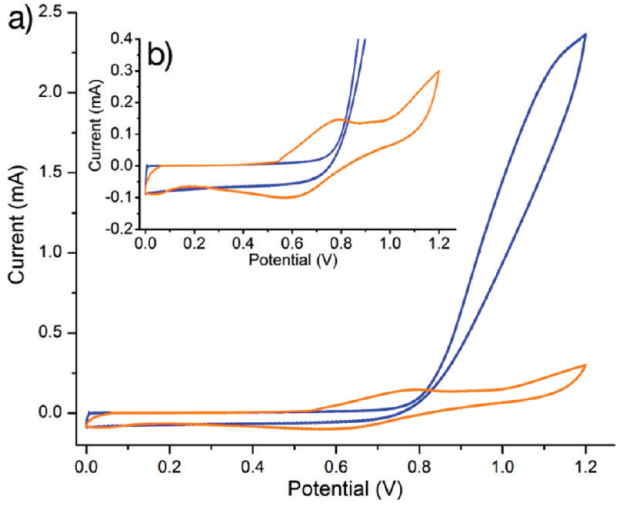

Figure 4. (a) Cyclic voltammetry graphs of MnO_2 (10 mM) and PEDOT (80 mM) growth on ring-shaped electrodes in an alumina template at a scan rate of 100 mV/s from 0 to 1.2 V. (b) Magnified view of MnO_2 cyclic voltammetry graph.

deposition. This also supports the formation mechanism of the coaxial nanowires stated earlier: a MnO_2 core is grown at the smooth inner surface of the ring, while a PEDOT shell is selectively grown on the sharp edge of the ring (Scheme 1a). The gradual thinning of the MnO_2 is caused by two possible reasons: First, the depletion of Mn^{2+} due to the limited diffusion of the Mn^{2+} ions at the low concentration and high over potential played a very important role. Once the Mn^{2+} is almost depleted, the PEDOT growth becomes overwhelming and deposits on the top of the MnO_2, which may prevent further growth of MnO_2 due to the aforementioned mutual exclusion of MnO_2 and PEDOT. Second, as the nanowires grow longer, the potential drop on the wire tips becomes greater, and this is especially true for the MnO_2 growth because the MnO_2 is less conductive than the PEDOT and the growth of MnO_2 becomes less and less.

It is worth noting that, when the potential is further increased for coelectrodeposition of MnO_2 and PEDOT on the flat-top electrodes, the MnO_2 segment on the flat-top electrode becomes shorter and may further be reduced to a "dome" shape, as shown in Figure 3b–d. This can be explained by the quicker depletion of Mn^{2+} driven by the higher over potential as well as faster coverage by the PEDOT on the top region.

Modifying the Structure of the Coaxial Nanowires. The excellent electrochemical properties of the MnO_2/PEDOT coaxial nanowires for their potential application as supercapacitor electrode materials were shown in our previous communication,[17] but it is still crucial to adjust the structure and composition of these coaxial nanowires to obtain the best electrochemical performance. Individual growth rates of MnO_2 and PEDOT, as well as MnO_2/PEDOT coelectrodeposition rates on the ring-shaped electrode, directly affect the structure and composition of the MnO_2/PEDOT nanowires and hence warrant both qualitative and quantitative analysis.

MnO_2 and PEDOT individual growth rates were analyzed on the ring-shaped electrode in the alumina template using CV methods, which are presented in Figure 4. Again, a 10 mM Mn^{2+} solution was used for MnO_2, while an 80 mM EDOT solution was used for PEDOT. The occurrence of symmetric peaks (Figure 4b) in the CV graph of MnO_2 deposition is due to the limited diffusion of the low concentration and the reversible electrochemistry of Mn^{2+} on the nanosized electrode surface (inner smooth surface of the ring-shaped electrode). Under a high concentration of Mn^{2+}, you will see the current continue to rise up with increased potential instead of a peak shape, which can be seen in the Supporting

Information, Figure S1. The position of the peaks indicates the oxidation potential of Mn^{2+} and the reduction potential of MnO_2 or other Mn species with higher oxidation valence status. The CV graph of PEDOT is much easier to understand. The onset growth potential occurs where the current sharply increases above 0.8 V due to the high concentration of EDOT monomer. As can be seen in Figure 4, the onset growth potential of MnO_2 (0.5 V) is significantly lower than that of PEDOT (0.8 V). This suggested that, below 0.7 V, the MnO_2 growth will be predominant, while above 0.85 V, the PEDOT growth will be overwhelming.[17]

Between the potential of 0.7 and 0.85 V, the resulting currents from MnO_2 and PEDOT deposition are comparable, which suggests that the structure of the coaxial nanowire and MnO_2/PEDOT ratio are very sensitive in this potential range. To reveal the MnO_2/PEDOT ratio and its relationship to MnO_2/PEDOT growth rates at different deposition potentials, potentiostatic methods were used to monitor the MnO_2, PEDOT, and MnO_2/PEDOT steady growth currents and additionally use EDS to determine the MnO_2/PEDOT ratio.

Table 1 lists the steady-state currents for the potentiostatic electrodeposition of individual components of MnO_2 (i_{MnO_2}) and PEDOT (i_{PEDOT}) as well as the current for MnO_2/PEDOT coelectrodeposition (i_{co}) in the alumina template. As can be seen in the table, the sum of the i_{PEDOT} and i_{MnO_2} corresponds closely with the observed i_{co} at 0.75 and 0.85 V. This provides additional evidence of the aforementioned mechanism. The growth of coaxial nanowires (related to i_{co}) can be explained as a process entailing the separate growth of the MnO_2 core (related to i_{MnO_2}) on the ring inner surface and of the PEDOT shell (related to i_{PEDOT}) on the ring edge. However, the i_{co} at higher potentials (0.85 V) only matches the i_{PEDOT}, which suggests the dominant growth of PEDOT quickly covers the edges and leads to the growth of solid PEDOT nanowires, which may exclude further deposition of MnO_2. We also list the experimentally observed Mn/S molar ratio by EDS and compare them with the Mn/S ratios predicted on the basis of the i_{PEDOT} and i_{MnO_2} values (please note 1 mol MnO_2 formation requires 1.7 mol electrons, while 1 mol of PEDOT formation needs 2.3 mol electrons), which can be obtained by

$$(Mn/S)_{current} = \frac{(i_{MnO_2}/1.7)}{(i_{PEDOT}/2.3)} \quad (1)$$

At 0.75 and 0.80 V, the $(Mn/S)_{current}$ corresponds closely with the $(Mn/S)_{EDS}$. However, at higher potentials, $(Mn/S)_{EDS}$ is much lower than $(Mn/S)_{current}$, which is due to the overwhelming growth of PEDOT, as stated earlier. At lower potentials, $(Mn/S)_{current}$ is lower than $(Mn/S)_{EDS}$. This is probably because the i_{PEDOT} measured at 0.6 and 0.70 V was larger than the real current contributed by PEDOT growth during the coelectrodeposition of the MnO_2/PEDOT coaxial nanowires. This could result due to the steady-state current of i_{PEDOT} being proportional to the electrode area, which can become larger when the PEDOT growth is not restricted to the edge of the ring-shaped electrode.

TABLE 1. Steady-State Currents of MnO_2 (i_{MnO_2}) and PEDOT (i_{PEDOT}) and the Current for Coelectrodeposited (i_{co}) MnO_2/PEDOT during Potentiostatic Electrodeposition in an Alumina Template[a]

potential (V)	i_{PEDOT} (μA)	i_{Mn} (μA)	$i_{PEDOT} + i_{MnO_2}$ (μA)	i_{co} (μA)	$(Mn/S)_{current}$	$(Mn/S)_{EDS}$
0.6	2	25	25	30	17	32
0.70	20	50	65	70	3.38	9
0.75	70	60	130	120	1.16	1.05
0.8	200	70	270	250	0.47	0.43
0.85	400	75	475	410	0.25	0.05
0.90	600	80	680	620	0.18	0.03
1.0	950	90	1010	980	0.13	0.01

[a] $(Mn/S)_{current}$ is the predicted molar ratio of MnO_2 to PEDOT based on i_{MnO_2} and i_{PEDOT}, resulting from their separate potentiostatic electrodepositions. $(Mn/S)_{EDS}$ is the experimentally observed Mn/S molar ratio.

The selective growth of MnO_2 and PEDOT at different potentials on the ring-shaped electrode suggests that segmented MnO_2/PEDOT nanowires can be fabricated if alternating potentials are applied during the electrodeposition, as illustrated in Scheme 2. To the best of our knowledge, this is the first report of such metal oxide/conductive polymer segmented nanowires. When a potential of 0.6 V is applied, MnO_2 is selectively grown due to the lower onset potential of MnO_2.[34,35] Whereas when 0.9 V is applied, only PEDOT is electrodeposited due to the dominant growth of PEDOT.

Similar work has been carried out to electrodeposit segmented nanowires with two different metals (Cu/Co[36] and Pt/Ni[37]) using different reduction potentials.[38] The more noble metal can be selectively deposited at a potential that is more positive than the reduction potential of the more active metal. The potential is then pulsed more negative to deposit the more active metal. The concentration of the second metal precursor ions in the plating solution is always much higher than the first metal precursor ions. This minimizes the deposition of the more noble first metal during the deposition of the second metal at the more negative potential; however, both of the metals will still coelectrodeposit.

This similar problem is avoided in the deposition of MnO_2/PEDOT segmented nanowire because PEDOT can inhibit the growth of MnO_2 due to depletion of Mn^{2+} and the mutual aversion of MnO_2 and PEDOT. The length of the MnO_2 and PEDOT can be controlled by adjusting the amount of charge passed during the electrodeposition. For example, the PEDOT segments in Figure 5b are controlled to be much shorter than the PEDOT segments in Figure 5a. An EDS line scan and a backscattered electron (BSE) SEM image of an array of segmented MnO_2/PEDOT nanowires can be seen in Supporting Information Figures S2 and S3, respectively.

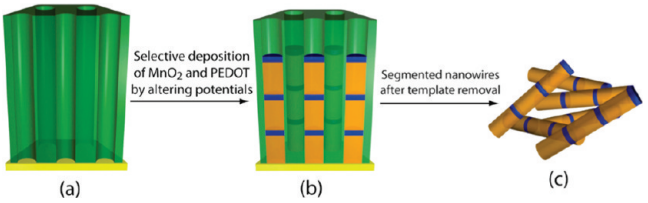

Scheme 2. Synthesis of segmented MnO_2/PEDOT nanowires *via* selectively deposited MnO_2 and PEDOT by application of alternating potentials.

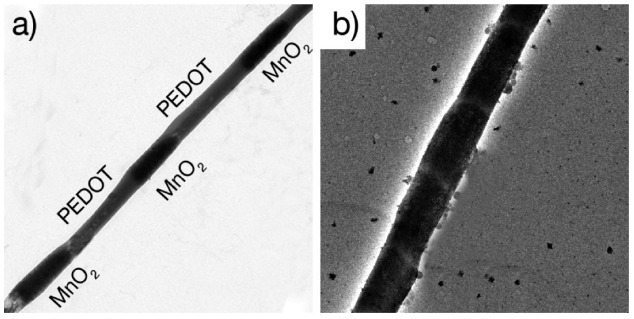

Figure 5. Segmented MnO_2/PEDOT nanowires electrodeposited by applying alternating potentials in a single bath of manganese acetate (10 mM) and EDOT (80 mM). (a) PEDOT and MnO_2 segments are electrodeposited by the same charge densities of 250 mC/cm^2 at 0.6 and 0.9 V. (b) Same synthetic conditions as (a) except PEDOT is electrodeposited at charge densities of 50 mC/cm^2.

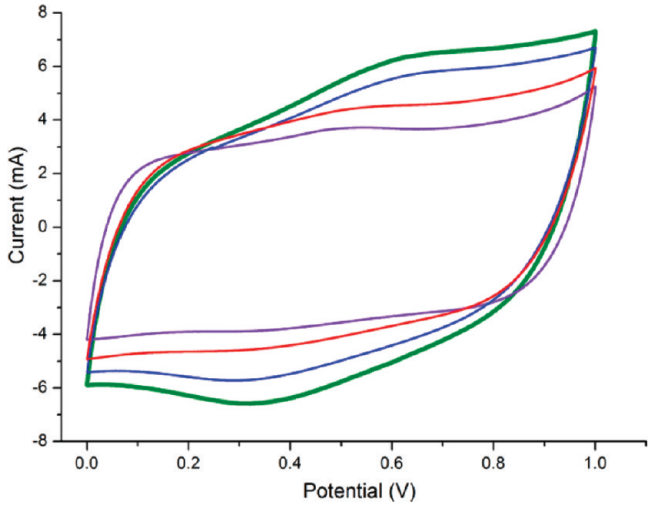

Figure 6. Cyclic voltammograms of MnO_2/PEDOT coaxial nanowires coelectrodeposited at potentials of 0.65 V (blue), 0.70 V (green), 0.75 V (red), and 0.80 V (purple) obtained at 250 mV/s in a solution of 1 M $LiClO_4$ with a potential window of 0−1 V.

The BSE image is able to show the contrast between elements of different atomic number. In this case, the bright segments represent the higher average atomic number of the elements in MnO_2, while the dark segments represent the lower average atomic number of the elements in PEDOT. The SEM shows that all of the nanowires produced in the array have the same segmented structure. These segmented nanowires can be a fundamental tool in the study of the properties of heterogeneous nanostructures.

Supercapacitor Characterization of Modified Coaxial Nanostructures. On the basis of the above results, we further investigated the electrochemical performance of MnO_2/PEDOT coaxial nanowires electrodeposited at different potentials in order to determine the best composition for electrochemical energy storage applications. Figure 6 shows CV graphs of coaxial nanowires deposited at 0.65, 0.70, 0.75, and 0.8 V. Here we named them as CoNW-065, CoNW-070, CoNW-075, and CoNW-080 for convenience. We divided the four CV curves into two groups (group I is CoNW-065 and CoNW-070; group II is CoNW-075 and CoNW-080) The capacitive current from group I is higher than that of group II due to a greater inclusion of MnO_2, which possesses a higher specific capacitance than PEDOT. However, the CV shape of group II is more rectangular, suggesting

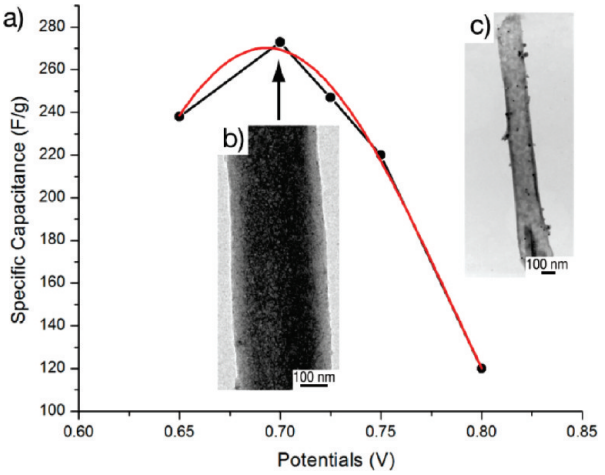

Figure 7. (a) Specific capacitance calculated from the CV graphs or galvanostatic charge–discharge curves for MnO_2/PEDOT coaxial nanowires deposited from 0.65, 0.70, 0.75, and 0.80 V. TEM images of (b) a coaxial nanowire obtained at a 0.70 V deposition potential, and (c) a PEDOT nanotube acquired upon etching of the MnO_2 core of nanowire obtained at a 0.70 V deposition potential.

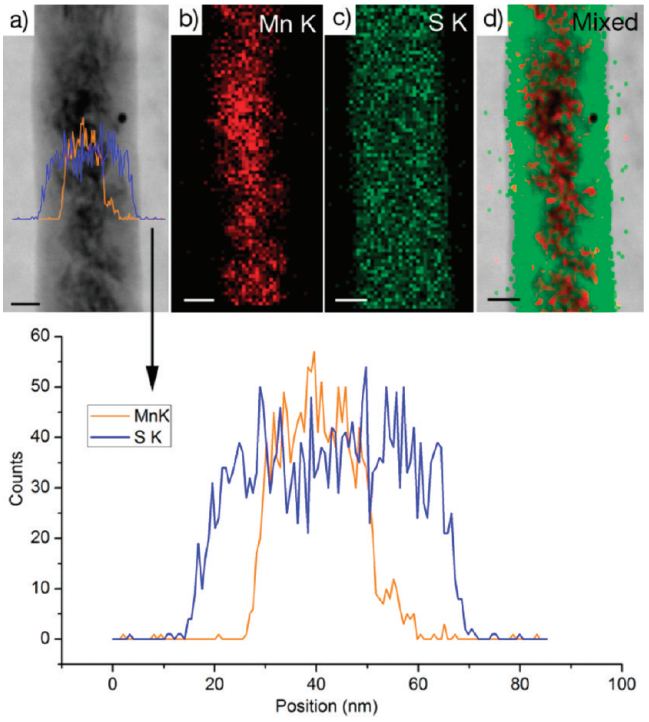

Figure 8. (a) TEM image of a MnO_2/PEDOT coaxial nanowire synthesized in a homemade template. (b) Mn, (c) S, and (d) mixed Mn and S EDS K-shell mapping of the same coaxial nanowire in (a). (e) Mn (orange) and S (blue) elemental EDS K-shell line scan profile across the same coaxial nanowire in (a).

a more ideal capacitive behavior due to a greater incorporation of the highly conductive PEDOT. Careful comparison of the CV curves from CoNW-065 and CoNW-070 reveals that the capacitive current from CoNW-070 is higher than that of CoNW-065.

Figure 7a shows the specific capacitance calculated from the CV graphs or galvanostatic charge–discharge curves (data not shown) of the CoNW-065, CoNW-070, CoNW-075, and CoNW-080 electrodeposited coaxial nanowires. Detailed calculation methods can be found in our previous paper.[17,32] The specific capacitance of the CoNW-070 is found to be the highest (270 F/g), which is consistent with the fact that the CoNW-070 has the highest capacitive current observed in Figure 6. This high specific capacitance is due to the minimal thickness of the PEDOT shell material, which provides high conductivities without a significant decrease in the amount of the highly energy dense MnO_2. At this potential, the PEDOT is observed as a thin shell, which can be seen in the coaxial images in panels b and c

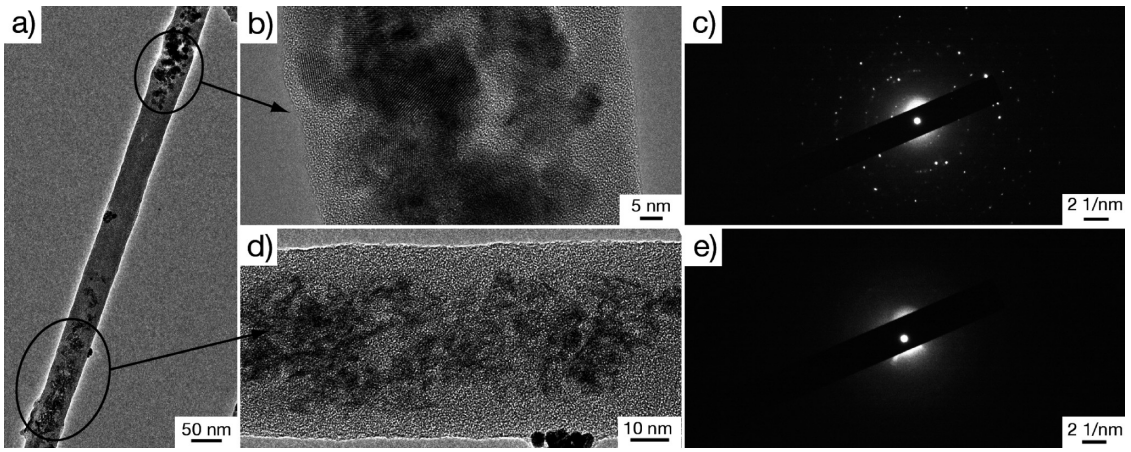

Figure 9. (a) TEM image of a heterogeneous MnO_2/PEDOT nanowire electrodeposited into a homemade AAO template. (b,d) TEM images of the different morphologies of the core MnO_2 found along the same nanowire in (a). (c,e) Corresponding electron diffraction patterns of the core MnO_2 found in images (b) and (d).

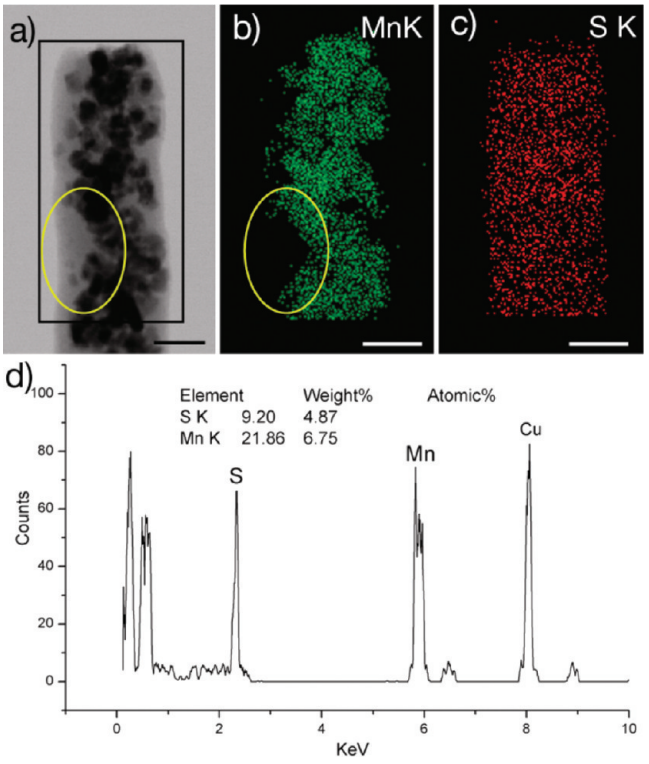

Figure 10. EDS analysis of MnO_2 nanoparticles encased in a PEDOT shell from the coelectrodeposition of MnO_2 and PEDOT in the small pore sized AAO. (a) TEM image of the coaxial nanowire. EDS mapping of (b) S, (c) Mn, and (d) mixed Mn and S using K-shell electrons. (d) Elemental weight percentage of Mn and S obtained from the EDS mapping. The yellow circle indicates the area where the PEDOT has a non-uniform wall thickness.

of Figure 7, where the core MnO_2 has been etched revealing thin-walled nanotubes of PEDOT.

MnO_2/PEDOT Coaxial Nanowire Growth in a Small Sized Template. Finally, we study the coelectrodeposition of MnO_2 and PEDOT in a homemade template, which was synthesized having a smaller pore diameter (50 nm) than the commercial alumina membrane (200 nm) obtained from Whatman Inc. The coelectrodeposited MnO_2 and PEDOT in the homemade template can be described as follows. The bottom electrodes formed from the sputtering of Au in the homemade template are relatively flatter compared to the sputtered electrode in a commercial membrane.[25] It is much more difficult for the sputtered Au to access the smaller diameter pores, which causes the edge of the ring-shaped electrode to be less sharp.

Consequently, it is more difficult for the PEDOT to be electrodeposited without the sharp edge, and the PEDOT growth onset potential is thus shifted to a higher potential, which was also observed on the flat-top electrodes as noted earlier. For example, PEDOT cannot be clearly

detected by EDS below 0.80 V. Meanwhile, at 0.85 V, a MnO_2/PEDOT coaxial structure is observed somewhat similar to those synthesized in the large pore size commercial membrane. Figure 8a shows a TEM image of the MnO_2/PEDOT coaxial nanostructure electrodeposited in the homemade template; the dark core represents the MnO_2, while the bright shell represents the PEDOT. The elemental maps of Mn, S, and the mixed map of Mn and S also confirm the coaxial structure. The Mn and S elemental line scan across the nanowire shows the precise positioning of MnO_2 and PEDOT in the nanowire.

It is worth noting that the coaxial nanostructure of MnO_2/PEDOT is not uniform along the whole axis of the homemade template synthesized nanowire. Coaxial nanostructures are randomly found at different locations along the axis of the nanowire. This could be explained by the limited diffusion of both the EDOT monomer (even at a higher concentration of 80 mM) and the Mn^{2+} ions in the small pore size membrane. For instance, when the EDOT starts to be depleted, the PEDOT begins to grow in a tubular-like morphology. After most of the EDOT in the small channel is consumed, MnO_2 starts to deposit on the inner surface of these PEDOT nanotubes to form a short coaxial MnO_2/PEDOT segment. However, the Mn^{2+} ions are quickly depleted due to their small concentration; the EDOT monomer concentration then recovers and starts to cover the previously grown MnO_2. Such alternating deposition is thus repeated to form these partial coaxial nanowires.

Another interesting observation is the varying morphologies of the core MnO_2 at different locations along the axis of the heterogeneous nanowires. The MnO_2 was analyzed by planar film XPS measurements (Supporting Information, Figure S4), which is similar for all of the MnO_2 synthesized in this paper, and confirms that the identity of MnO_2 as the valence status of Mn is 4. Figure 9a shows a typical TEM image of a MnO_2/PEDOT coaxial nanowire coelectrodeposited in the small diameter template (50 nm). Figure 9b,d illustrates the different morphologies of the core MnO_2 along the axis of the same nanowire. Figure 9b shows the MnO_2 in the form of nanoparticles with sizes of 10−20 nm. The EDS mapping of a similar area can be found in Figure 10. The high-resolution TEM clearly shows these nanoparticles have crystalline structures, which is also verified in the electron diffraction pattern in Figure 9c. Figure 9d reveals the MnO_2 morphology of the MnO_2 core material at a different location along the nanowire. The MnO_2 at this location displays the typical fiber-like morphology observed in the large pore size membrane.[17] From the high-resolution TEM, no crystal structures can be found on these MnO_2 nanofibers, and no dots or rings can be found in the electron diffraction pattern (Figure 9e) of this MnO_2 nanofiber area, which suggests their amorphous nature.

CONCLUSION

The mechanism of the coelectrodeposition of coaxial MnO_2/PEDOT nanowires has been studied here in detail by performing the coelectrodeposition of MnO_2 and PEDOT on nanoelectrodes with different shapes (ring and flat) inside alumina template channels. The sharp edge on the ring-shaped electrode is found to play a crucial role in initiating the growth of the PEDOT nanotube shell, while the flat-top electrode is more favorable for the deposition of MnO_2. The growth of these coaxial nanowires involves the parallel growth of core MnO_2 on the smooth inner surface and shell PEDOT on the sharp edges of the ring-shaped nanoelectrode. The electrodeposition potential exerts significant influence on the structure and composition of these MnO_2/PEDOT nanowires. As for ring-shaped electrodes, above 0.90 V, only PEDOT is synthesized, while below 0.60 V, only MnO_2 is synthesized. Subsequently, for the first time, segmented MnO_2/PEDOT nanowires with different lengths of MnO_2 and PEDOT were fabricated by altering the electrochemical deposition potential. Between 0.60 and 0.90 V, coaxial nanowires are formed with differing thicknesses of the PEDOT shell. In this study, 0.70 V is found to be the ideal condition to electrodeposit MnO_2/PEDOT coaxial nanowires for supercapacitor applications with an optimal specific capacitance of 270 F/g. Finally, in the smaller pore sized membrane, MnO_2 and PEDOT are found to be partially assembled into coaxial nanowires due to the alternative depletion of Mn(II) ions and EDOT monomer molecules.

The formation mechanism of MnO_2/PEDOT coaxial nanowires and the synthetic methods for other heterogeneous MnO_2/PEDOT nanostructures presented in this paper offers new insights into the electrosynthesis of materials at nanoscale electrodes and expands the investigative scope of template synthesized heterostructured nanomaterials in general. This example of optimizing the composition and structure of the coaxial MnO_2/PEDOT nanowires for their best electrochemical performance provides important guidance for building high-power (high conductivity) and high-energy (high capacitance) heterogeneous nanomaterials for electrochemical energy storage devices.

METHODS

Chemicals and Materials. 3,4-Ethylenedioxythiopene (EDOT), manganese acetate, and lithium perchlorate ($LiClO_4$) were purchased from Sigma Aldrich (Milwaukee, WI). Sodium dodecyl sulfate was obtained from Fisher Scientific (Fair Lawn, NJ). Deionized water (*ca.* 18 MΩ·cm resistivity) was made by a

Milli-Q water purification system (Millipore; Dubuque, IA). Alumina membranes of 200 nm pore diameter and 60 μm thickness are commercially available from Whatman (Clifton, NJ). An alumina template with a pore diameter of *ca.* 50 nm was fabricated by using a two-step anodization process. This process can be briefly outlined as follows: An electropolished aluminum foil (99.99%, Alfa Aesar) was anodized at 40 V and 10 °C by using 0.3 M oxalic acid as an electrolyte. This generated an alumina layer with irregular pores. For better pore structures, this porous alumina layer was removed by using an aqueous mixture of phosphoric acid (6 wt %) and chromic acid (1.8 wt %), which exposed a barrier layer with a well-defined prepattern. The second anodization was performed as in the first anodization to generate well-defined pores until a desired thickness (*ca.* 100 μm) was reached. After the residual aluminum was dissolved using a mixture of 0.5 M $CuCl_2$ and 37% HCl aqueous solution, the removal of the alumina barrier layer and pore widening were performed by using phosphoric acid (5 wt %) at 30 °C for 80 min.

Synthesis. The preparation of a working electrode is as follows: First, a thin layer of gold (*ca.* 500 nm) was sputtered onto the branched side of an alumina membrane by using a sputtering system (Denton Vacuum Desktop III). The Au-coated membrane was connected to an electrical circuit using a copper tape (3M). Defining and sealing an electroactive window (0.32 cm^2 in nominal area) was performed using silicone rubber or Parafilm. Considering the porosity of the membrane (60%), the corrected surface area of the electroactive window was 0.2 cm^2.

Coelectrodeposition of the heterostructured MnO_2/PEDOT nanowires on ring-shape and flat-top nanoelectrodes in different pore size AAO membranes was performed potentiostatically between 0.6 and 1.0 V in an aqueous solution of 10 mM manganese acetate, 80 mM EDOT, 100 mM $LiClO_4$, and 140 mM SDS (pH = 6.5). The ring-shaped gold nanoelectrode is formed during the sputtering of gold. Gold bottoms for flat-top electrodes were electrochemically deposited at a current density of -1 mA/cm^2 for 30 min in an Orotemp 24 gold plating solution. All electrode potentials were measured relative to a Ag/AgCl reference electrode using a Pt foil as a counter electrode, if not specified otherwise. The mass and the length of the resulting heterogeneous nanowires or MnO_2 and PEDOT segments were controlled by fixing the total charge passed during the electrodeposition. Diameters of these nanowires corresponded to the pore diameters of the alumina template.

Characterizations. The heterogeneous MnO_2/PEDOT nanowires were investigated using a field-emission scanning electron microscope (Hitachi SU-70 SEM operated at an accelerating voltage of 10 keV) and a transmission electron microscope (JEOL TEM 2100 field emission transmission electron microscope (FE-TEM) at 200 keV). Briefly, the sampling methods for the SEM and TEM analyses are as follows: the gold-coated side of a small piece of alumina template was tightly attached onto an SEM specimen holder by using a carbon tape. The template was dissolved to expose the nanowires by using 3 M NaOH. After rinsing the sample with deionized water repeatedly, it was then dried in air prior to observation. For TEM sampling, sonication was applied to the heterostructured MnO_2/PEDOT nanowires in order to disperse them in ethanol. The released nanowires were repeatedly rinsed with deionized water and ethanol. Then, 6 μL of the nanowire solution was dropped and dried on a TEM grid.

In order to calculate specific capacitance, cyclic voltammetry at different scan rates (50−500 mV/s) and galvanostatic charge/discharge tests at different current densities (10−50 mA/cm^2) were performed by cycling the potential from 0 to 1 V in an aqueous 1 M $LiClO_4$ solution. The detailed calculation method can be found elsewhere.[17] All of the above electrochemical experiments were performed using a bipotentiostat (BI-STAT; Princeton Applied Research).

Acknowledgment. The work was supported by the Laboratory for Physical Sciences (R.L. and J.D.) and was also supported as part of the Science of Precision Multifunctional Nanostructures for Electrical Energy Storage, an Energy Frontier Research Center funded by the U.S. Department of Energy, Office of Science, Office of Basic Energy Sciences under Award Number DESC0001160 (J.D.). S.B.L. would like to thank the support of the WCU program of the KOSEF funded by the MEST (Grant No. R31-2008-000-10071-0). We thank Li-Chung Lai (NISP Lab) for assistance with SEM, SEM, and EDS analyses. We also thank Xinyi Chen very much for his help with the XPS analysis.

Supporting Information Available: Cyclic voltammetry graph of a high concentration of Mn^{2+} on the ring-shaped electrode. EDS line scan of a segmented nanowire. Backscattered SEM image of an array of segmented nanostructures. XPS spectrum of Mn from electrodeposited MnO_2. This material is available free of charge *via* the Internet at http://pubs.acs.org.

REFERENCES AND NOTES

1. Tarascon, J. M.; Armand, M. Issues and Challenges Facing Rechargeable Lithium Batteries. *Nature* **2001**, *414*, 359–367.
2. Kang, K. S.; Meng, Y. S.; Breger, J.; Grey, C. P.; Ceder, G. Electrodes with High Power and High Capacity for Rechargeable Lithium Batteries. *Science* **2006**, *311*, 977–980.
3. Service, R. F. Materials Science—New 'Supercapacitor' Promises To Pack More Electrical Punch. *Science* **2006**, *313*, 902–902.
4. Simon, P.; Gogotsi, Y. Materials for Electrochemical Capacitors. *Nat. Mater.* **2008**, *7*, 845–854.
5. Futaba, D. N.; Hata, K.; Yamada, T.; Hiraoka, T.; Hayamizu, Y.; Kakudate, Y.; Tanaike, O.; Hatori, H.; Yumura, M.; Iijima, S. Shape-Engineerable and Highly Densely Packed Single-Walled Carbon Nanotubes and Their Application as Super-Capacitor Electrodes. *Nat. Mater.* **2006**, *5*, 987–994.
6. Winter, M.; Brodd, R. J. What Are Batteries, Fuel Cells, and Supercapacitors? *Chem Rev.* **2004**, *104*, 4245–4269.
7. Whittingham, M. S. Lithium Batteries and Cathode Materials. *Chem. Rev.* **2004**, *104*, 4271–4301.
8. Long, J. W.; Dunn, B.; Rolison, D. R.; White, H. S. Three-Dimensional Battery Architectures. *Chem. Rev.* **2004**, *104*, 4463–4492.
9. Zhou, H. S.; Li, D. L.; Hibino, M.; Honma, I. A Self-Ordered, Crystalline-Glass, Mesoporous Nanocomposite for Use as a Lithium-Based Storage Device with Both High Power and High Energy Densities. *Angew. Chem., Int. Ed.* **2005**, *44*, 797–802.
10. Arico, A. S.; Bruce, P.; Scrosati, B.; Tarascon, J. M.; Van Schalkwijk, W. Nanostructured Materials for Advanced Energy Conversion and Storage Devices. *Nat. Mater.* **2005**, *4*, 366–377.
11. Bruce, P. G.; Scrosati, B.; Tarascon, J. M. Nanomaterials for Rechargeable Lithium Batteries. *Angew. Chem., Int. Ed.* **2008**, *47*, 2930–2946.
12. Guo, Y. G.; Hu, J. S.; Wan, L. J. Nanostructured Materials for Electrochemical Energy Conversion and Storage Devices. *Adv. Mater.* **2008**, *20*, 2878–2887.
13. Cheng, F.; Tao, Z.; Liang, J.; Chen, J. Template-Directed Materials for Rechargeable Lithium-Ion Batteries. *Chem. Mater.* **2008**, *20*, 667–681.
14. Wang, Y.; Cao, G. Z. Developments in Nanostructured Cathode Materials for High-Performance Lithium-Ion Batteries. *Adv. Mater.* **2008**, *20*, 2251–2269.
15. Patil, A.; Patil, V.; Shin, D. W.; Choi, J. W.; Paik, D. S.; Yoon, S. J. Issue and Challenges Facing Rechargeable Thin Film Lithium Batteries. *Mater. Res. Bull.* **2008**, *43*, 1913–1942.
16. Cahen, S.; Janot, R.; Laffont-Dantras, L.; Tarascon, J. M. Chemical Reduction of $SiCl_4$ for the Preparation of Silicon−Graphite Composites Used as Negative Electrodes in Lithium-Ion Batteries. *J. Electrochem. Soc.* **2008**, *155*, A512–A519.
17. Liu, R.; Lee, S. B. MnO_2/Poly(3,4-ethylenedioxythiophene) Coaxial Nanowires by One-Step Coelectrodeposition for Electrochemical Energy Storage. *J. Am. Chem. Soc.* **2008**, *130*, 2942–2943.
18. Reddy, A. L. M.; Shaijumon, M. M.; Gowda, S. R.; Ajayan, P. M. Coaxial MnO_2/Carbon Nanotube Array Electrodes for High-Performance Lithium Batteries. *Nano Lett.* **2009**, *9*, 1002–1006.

19. Kim, D. W.; Hwang, I. S.; Kwon, S. J.; Kang, H. Y.; Park, K. S.; Choi, Y. J.; Choi, K. J.; Park, J. G. Highly Conductive Coaxial SnO_2—In_2O_3 Heterostructured Nanowires for Li Ion Battery Electrodes. *Nano Lett.* **2007**, *7*, 3041–3045.
20. Kwon, Y.; Kim, H.; Doo, S. G.; Cho, J. H. $Sn_{0.9}Si_{0.1}$/Carbon Core—Shell Nanoparticles for High-Density Lithium Storage Materials. *Chem. Mater.* **2007**, *19*, 982–986.
21. Xie, H. M.; Wang, R. S.; Ying, J. R.; Zhang, L. Y.; Jalbout, A. F.; Yu, H. Y.; Yang, G. L.; Pan, X. M.; Su, Z. M. Optimized $LiFePO_4$-Polyacene Cathode Material for Lithium-Ion Batteries. *Adv. Mater.* **2006**, *18*, 2609–2613.
22. Liu, R.; Duay, J.; Lee, S. B. Redox Exchange Induced MnO_2 Nanoparticle Enrichment in Poly(3,4-ethylenedioxythiophene) Nanowires for Electrochemical Energy Storage. *ACS Nano* **2010**, *4*, 4299–4307.
23. Liu, R.; Duay, J.; Lee, S. B. Heterogeneous Nanostructured Electrode Materials for Electrochemical Energy Storage. *Chem. Commun.* **2011**, *47*, 1384–1404.
24. Il Cho, S.; Lee, S. B. Fast Electrochemistry of Conductive Polymer Nanotubes: Synthesis, Mechanism, and Application. *Acc. Chem. Res.* **2008**, *41*, 699–707.
25. Xiao, R.; Il Cho, S.; Liu, R.; Lee, S. B. Controlled Electrochemical Synthesis of Conductive Polymer Nanotube Structures. *J. Am. Chem. Soc.* **2007**, *129*, 4483–4489.
26. Hu, C. C.; Chang, K. H.; Lin, M. C.; Wu, Y. T. Design and Tailoring of the Nanotubular Arrayed Architecture of Hydrous RuO_2 for Next Generation Supercapacitors. *Nano Lett.* **2006**, *6*, 2690–2695.
27. Li, Q. G.; Olson, J. B.; Penner, R. M. Nanocrystalline α-MnO_2 Nanowires by Electrochemical Step-Edge Decoration. *Chem. Mater.* **2004**, *16*, 3402–3405.
28. Che, G. L.; Lakshmi, B. B.; Fisher, E. R.; Martin, C. R. Carbon Nanotubule Membranes for Electrochemical Energy Storage and Production. *Nature* **1998**, *393*, 346–349.
29. Sides, C. R.; Croce, F.; Young, V. Y.; Martin, C. R.; Scrosati, B. A High-Rate, Nanocomposite $LiFePO_4$/Carbon Cathode. *Electrochem. Solid-State Lett.* **2005**, *8*, A484–A487.
30. Li, N. C.; Martin, C. R.; Scrosati, B. Nanomaterial-Based Li-Ion Battery Electrodes. *J. Power Sources* **2001**, *97—8*, 240–243.
31. Li, N. C.; Patrissi, C. J.; Che, G. L.; Martin, C. R. Rate Capabilities of Nanostructured $LiMn_2O_4$ Electrodes in Aqueous Electrolyte. *J. Electrochem. Soc.* **2000**, *147*, 2044–2049.
32. Liu, R.; Il Cho, S.; Lee, S. B. Poly(3,4-ethylenedioxythiophene) Nanotubes as Electrode Materials for a High-Powered Supercapacitor. *Nanotechnology* **2008**, *19*, 215710.
33. Liu, R.; Duay, J.; Lane, T.; Lee, S. B. Synthesis and Characterization of RuO_2/Poly(3,4-ethylenedioxythiophene) Composite Nanotubes for Supercapacitors. *Phys. Chem. Chem. Phys.* **2010**, *12*, 4309–4316.
34. Chang, J. K.; Tsai, W. T. Material Characterization and Electrochemical Performance of Hydrous Manganese Oxide Electrodes for Use in Electrochemical Pseudocapacitors. *J. Electrochem. Soc.* **2003**, *150*, A1333–A1338.
35. Wu, M. S.; Chiang, P. C. J. Fabrication of Nanostructured Manganese Oxide Electrodes for Electrochemical Capacitors. *Electrochem. Solid-State Lett.* **2004**, *7*, A123–A126.
36. Piraux, L.; George, J. M.; Despres, J. F.; Leroy, C.; Ferain, E.; Legras, R.; Ounadjela, K.; Fert, A. Giant Magnetoresistance in Magnetic Multilayered Nanowires. *Appl. Phys. Lett.* **1994**, *65*, 2484–2486.
37. Liang, H. P.; Guo, Y. G.; Hu, J. S.; Zhu, C. F.; Wan, L. J.; Bai, C. L. Ni—Pt Multilayered Nanowire Arrays with Enhanced Coercivity and High Remanence Ratio. *Inorg. Chem.* **2005**, *44*, 3013–3015.
38. Mieszawska, A. J.; Jalilian, R.; Sumanasekera, G. U.; Zamborini, F. P. The Synthesis and Fabrication of One-Dimensional Nanoscale Heterojunctions. *Small* **2007**, *3*, 722–756.